Fuel 404 (2026) 136134

Contents lists available at ScienceDirect

Fuel

journal homepage: www.elsevier.com/locate/jfue

Full length article

Improving anti-oxidation properties of metal interconnects in solid oxide fuel cells via a dense Ag-based coating layer

Gongmei Yang[a,b], Andrew Potter[a], Joy Sumner[c,*]

[a] Faculty of Engineering and Applied Sciences, Cranfield University, Bedfordshire, United Kingdom
[b] School of Material Science and Engineering, Jiangsu University, Zhenjiang, Jiangsu, China
[c] Swinburne Institute of Technology, Hawthorn, Victoria, Australia

HIGHLIGHTS

- A high conductivity Ag-containing coating was successfully prepared.
- The dense protective coating slows the interconnect's oxidation.
- The coating effectively mitigated the increase in area-specific resistance.
- Pure metal coatings offer a new approach for interconnects.

ARTICLE INFO

Keywords:
Solid oxide fuel cells
Metallic interconnects
Ag coating
Oxidation
Cr poisoning

ABSTRACT

Solid Oxide Fuel Cells (SOFCs) are a highly efficient energy conversion technology, but the degradation of metal interconnects remains a critical challenge. Conventional coatings often lack sufficient electrochemical performance and stability. In this study, a dense Ag coating was developed using the screen-printing method to improve the electrochemical performance and chemical compatibility of SOFC interconnects. Symmetric and single cells were prepared with $La_{0.6}Sr_{0.4}Co_{0.2}Fe_{0.8}O_{3-\delta}$ cathodes and SUS430 interconnects to evaluate the coating under high-temperature conditions, simulating real SOFC operation. The Ag coating demonstrated excellent adhesion, uniformity, and oxidation resistance, with conductivity increasing from 0.01 to 13.13 S cm^{-1} at 650 °C after coating and the area-specific resistance decreasing from 1.843 to 0.378 Ω cm^2 after coating between cathode and interconnect at 750 °C. Moreover, the coating effectively inhibited Cr diffusion from the interconnect to the cathode, addressing a major limitation in SOFC durability. These results suggest that Ag coatings offer a practical and promising solution to enhance the performance and extend the lifespan of SOFC systems.

1. Introduction

Solid Oxide Fuel Cells (SOFCs), as high-temperature fuel cells, can achieve up to 75 % efficiency [1,2]. They offer fuel flexibility and reduced carbon emissions [3–5], making them a promising solution for clean and sustainable energy. In SOFC stacks, interconnects play a vital role by electrically and mechanically connecting individual cells (consisting of cathode, anode, and electrolyte) [6], which enable the development of scalable and efficient energy systems.

Metallic materials have become promising candidates for interconnects due to their excellent electrical conductivity, high mechanical strength, and cost-effectiveness [7,8]. Among them, ferritic stainless steels (FSS) are widely considered for SOFC interconnects because their thermal expansion coefficients match those of other SOFC components, and they offer reasonable manufacturing costs [6,9]. However, the high operating temperatures (500–800 °C) pose a significant challenge for FSS interconnects, primarily due to the formation of a Cr-rich oxide layer. Although this oxide layer initially provides short-term oxidation protection, it gradually increases electrical resistance as it grows thicker during prolonged operation. Over time, oxide spallation can occur, accelerating interconnect degradation [10]. Moreover, in the humid and high-temperature environment of SOFCs, Cr volatilization becomes a critical issue. The released Cr species can poison the cathode, degrading its electrochemical performance [11]. These volatile Cr compounds deposit on the cathode surface, blocking active sites and impairing the

* Corresponding author.
Email address: jsumner@swin.edu.au (J. Sumner).

https://doi.org/10.1016/j.fuel.2025.136134
Received 7 March 2025; Received in revised form 13 June 2025; Accepted 25 June 2025
Available online 5 July 2025
0016-2361/© 2025 The Authors. Published by Elsevier Ltd. This is an open access article under the CC BY license (http://creativecommons.org/licenses/by/4.0/).

oxygen reduction reaction (ORR), which is essential for efficient cell operation [12,13].

To address these issues, various coating strategies have been explored to prevent Cr diffusion, decrease area-specific resistance (ASR), and extend the service life of FSS [14,15].

Researchers have proposed various coating solutions for SOFC interconnects. Metal oxides are considered the most commonly studied type of interconnect coating, especially perovskite-structured metal oxides [16,17] and spinel-structured metal oxides [18,19] because of their excellent thermal and chemical stability. To achieve uniform and dense coatings with enhanced adhesion and stability, various techniques such as screen printing [20], thermal spraying [21], physical vapor deposition (PVD) [19,22], and electrophoretic deposition (EPD) [23,24] are being explored. Screen printing can produce uniform and high-quality coatings, enhance the conductivity and corrosion resistance of interconnects, and can also be cost-effective for large-scale applications [25].

Although metal oxide coatings effectively alleviate FSS failure, their primary limitation lies in the growth of a low-conductivity chromia layer at the steel/coating interface [6]. Developing alternative coating materials with both high conductivity and high density at elevated temperatures presents a potential solution. Ag ranks among the most electrically conductive metals, with a conductivity of 3.67×10^7 S m^{-1} at 600 °C [26]. Researchers have explored modification of SOFC electrode materials with highly conductive Ag in the form of composite coatings or nano doping to enhance the efficiency and stability of SOFCs [23,27–31]. Significant advancements in this area include the development of composite coatings that integrate Ag with lanthanum strontium cobalt ferrite and samarium-doped ceria carbonate (SDCC), demonstrating good thermal compatibility with SUS430 stainless steel. Studies by Linda et al. [27] and Omar et al. [23] have made substantial con tributions to this field, highlighting the potential of these composite coatings.

Recent studies have underscored several important applications of Ag coatings in SOFCs. For instance, Zhu et al. [28] and Kim et al. [29] applied nano-Ag particles to modify the cathode material of low-temperature SOFCs. This effective strategy marked a milestone for achieving excellent SOFC cathode performance under mid-to-low temperature conditions. High-conductive Ag adhesives as collectors are employed in SOFCs to connect the electrodes and electrolyte, significantly reducing interfacial resistance and improving overall cell efficiency [30,31]. These adhesives offer excellent electrical conductivity and stability at high temperatures, making them ideal for SOFC applications. However, current Ag coatings face limitations in SOFC interconnect applications due to high-temperature volatility, poor densification, and high costs [6]. While existing studies predominantly adopt low-conductivity oxide coatings (e.g., $LaCrO_3$, $MnCo_2O_4$), these compromise interfacial performance [11]. This study innovatively proposes an Ag-based coating combined with a screen printing and gradient sintering process. By maintaining high electrical conductivity while achieving high densification, the interfacial resistance is reduced by over fivefold compared to pre-coated components.

Overall, the application of Ag as a diffusion barrier in SOFCs represents a promising approach to enhancing the performance and efficiency of these devices. The challenge of maintaining Ag's density at high temperatures (500–800 °C), along with concerns about its durability due to volatility at these temperatures. Continued research in this field is crucial to overcoming existing challenges and realizing the full potential of Ag in SOFC technology.

In this study, we have pioneered the use of high-conductive Ag adhesives as a coating for interconnects in SOFCs; improving conductivity while slowing down the oxidation of FSS in the SOFC working environment, thus forming a dense barrier layer to reduce the toxicity of Cr emitted from FSS to the SOFC cathode. For a detailed investigation of electrochemical performance, a single cell with a $La_{0.6}Sr_{0.4}Co_{0.2}Fe_{0.8}O_{3-\delta}$ (LSCF) cathode was assembled to show the effectiveness of coatings. Based on this experimental configuration, a systematic investigation of oxidation behavior and electrical properties of bare and coated steels under SOFC operating temperature has been conducted to verify the feasibility of this approach. By examining these aspects, the paper can reveal the usefulness of Ag technology in enhancing the durability and performance of metallic interconnects in SOFC applications.

The remainder of this paper is structured as follows: Section 2 will cover the material preparation methods and characterization techniques. Section 3 will provide an in-depth discussion on the Ag coating, including surface analysis (Section 3.1), oxide layer structure (Section 3.2), conductivity and ASR (Section 3.3), output power and stability in SOFC single cell systems (Section 3.4), Cr diffusion (Section 3.5), and lifetime prediction of the coating (Section 3.6). The feasibility of using Ag coatings for SOFC interconnects will be thoroughly evaluated.

2. Experimental section

2.1. Preparation of Ag coating by the screen printing method

For oxidation testing, samples were prepared. DAD-87 conductive Ag adhesives (including 82 % Ag, epoxy resin, and phenolic resins), sourced from Shanghai Research Institute of Synthetic Resins Co., Ltd., were used in this study. Alpha-terpineol served as a diluent to adjust the paste's viscosity for screen printing. The mass ratio of Ag adhesive to alpha-terpineol was maintained at 10:1.

Circular cylindrical samples of SUS430 stainless steel, measuring 14 mm in diameter and 3 mm in thickness, were prepared. The chemical composition of the alloy is listed in Table S1. Before the Ag coating application, the samples underwent 20 min of ultrasonic cleaning to remove particulate contamination. This was followed by wiping the surfaces with acetone and ethanol to eliminate any residual oils. The diluted Ag paste was then applied to the clean surface of each SUS430 sample using a screen printing method for uniform application (Fig. S1). The coated samples were dried in an oven at 80 °C for 2 h to remove the solvent and ensure good adhesion. Subsequently, the samples were sintered in a muffle furnace at 900 °C for 2 h to enhance the densification and durability of the Ag coating on the stainless steel substrate.

2.2. Exposure testing equipment and conditions

The samples were placed in a specially designed exposure unit to maintain a controlled environment for high-temperature exposure testing in single atmosphere, as shown in Fig. S2. They were exposed to humid air at 750 °C for 50, 100, or 200 h. The gas flow rate was set at 80 mL min^{-1}, and bubbled through bottles of pure water kept at a constant temperature of 25 °C to ensure a 3 % H_2O concentration prior to entering the furnace. Table 1 lists the names of all samples along with their corresponding experimental conditions, including atmosphere, gas flow, exposure/heat time, and temperature.

Table 1
Experimental conditions for sample preparation and later exposure to air with 3 % H_2O.

Name	Coating	Cathode	Heat treatment	Exposure/heat time (h)	Temperature (°C)
430 0 h	–	–	–	–	–
430 50 h	–	–		50	750
430 100 h	–	–		100	750
430 200 h	–	–		200	750
As deposited	Ag	–	–	–	–
Coated 0 h	Ag	–	900 °C 2 h	–	–
Coated 50 h	Ag	–	900 °C 2 h	50	750
Coated 100 h	Ag	–	900 °C 2 h	100	750
Coated 200 h	Ag	–	900 °C 2 h	200	750
430 + Ag	Ag	–	900 °C 2 h	–	750
430 + LSFC	–	LSCF	900 °C 2 h	–	750
430 + Ag + LSFC	Ag	LSCF	900 °C 2 h	–	750

2.3. Composition and structural characterization

The morphology and cross-sectional analysis of the sample were performed using a field emission scanning electron microscope (FE-SEM, TESCA VEGA 4) equipped with energy-dispersive X-ray spectroscopy (EDS). The phase structures of the metal and oxide layers were characterized using X-ray diffraction (XRD, SIEMENS D500D) with Cu Kα radiation. Data were collected over a 2θ range of 10–90°, with a step size of 0.05°. Sintered interconnects' surface elemental compositions were examined using X-ray photoelectron spectroscopy (XPS, Thermo ESCALAB 250).

2.4. Fabrication of cell with interconnect

To collect electrochemical data, cells were fabricated. The cathode material, $La_{0.6}Sr_{0.4}Co_{0.2}Fe_{0.8}O_{3-\delta}$, was synthesized by the sol-gel method, as shown in Fig. S3. Using a ball mill, a homogeneous cathode slurry was prepared by milling LSCF powder with ethyl cellulose and alpha-terpineol in a mass ratio of 1:0.06:0.94 [32]. An anode-supported electrolyte, manufactured by Haechi (Beijing) Information Technology Co., Ltd, was used to make a single cell. This cathode slurry was screen-printed onto the electrolyte discs to form a uniform layer, dried, and then sintered at 900 °C for 4 h with a heating rate of 2 °C min^{-1} to ensure proper adhesion and microstructural development.

Symmetrical cells were constructed using laboratory-manufactured gadolinium-doped ceria (GDC) discs as substrates. LSCF cathode paste was applied to both sides of these GDC discs following a method outlined in referenced literature [33], using screen printing to ensure consistency. After printing, the discs were sintered at 900 °C for 4 h to complete the formation of the symmetrical cells. The effective electrode area on each side was defined by a circle with a diameter of 6 mm.

2.5. Electrical properties

The ASR based on SUS430 interconnects was measured using the direct current four-probe technique. Refer to the inset diagram in Fig. 4b for the test schematic. The electrochemical performance of single cells, using the interconnect as a current collector, was evaluated using an electrochemical workstation (S1260 + S1287, Solartron Analytical). Electrochemical Impedance Spectroscopy (EIS) measurements were conducted over a frequency range from 10^{-6} to 10^{-2} Hz with a bias voltage of 20 mV. The I–V curves of the single cells were recorded by gradually increasing the scan voltage from 0.1 V to 1.1 V, at a scan rate of 10 mV s^{-1}. The single cells were sealed at the top of an alumina ceramic tube using ceramic adhesive to ensure airtight conditions during the tests. This arrangement is essential to prevent gas leakage and to maintain the integrity of the cell environment. During testing, a mixture of nitrogen and hydrogen gases was injected at the anode, while compressed air was supplied to the cathode.

2.6. Quality loss of Ag coatings

The coating was prepared using the screen printing method described in Section 2.1, applied to a smooth mold with a diameter of 2 cm to achieve a thickness of approximately 1.5 mm. After drying in an oven at 80 °C, the coating was carefully removed from the mold and calcined at 900 °C for 2 h, resulting in a silver-containing disk with a diameter of 1.87 cm and a thickness of 1.49 mm. The initial weight of the coating disk was measured using an analytical balance. The disk was then exposed to the environment described in Section 2.2 for durations of 50 h, 150 h, and 300 h. After each exposure period, the weight of the coating disk was measured again. The mass loss and volatilization rate were calculated based on the initial and post-exposure weights, using the formulas:

$$\text{Mass Loss (\%)} = \left(\frac{\text{Initial Weight} - \text{Final Weight}}{\text{Initial Weight}}\right) \times 100 \quad (1)$$

$$\text{Volatilization Rate} = \frac{\text{Mass Loss}}{\text{Exposure Time}} \quad (2)$$

3. Results and discussion

3.1. Microstructure of Ag coating

Fig. 1 provides insight into the microstructural evolution of the surface of the Ag coatings on the interconnect. SEM (Fig. 1a–c) highlights significant changes in the surface morphology of the Ag coatings. In Fig. 1a, the Ag coating (as deposited) exhibits a rough and granular surface, indicative of a densely packed but loosely bound particulate structure. This morphology is characteristic of coatings that have not undergone heat treatment, showing distinguishable and relatively non-fused individual Ag particles. After heat treatment at 900 °C for 2 h (Fig. 1b), the surface undergoes substantial transformation. The high-temperature treatment leads to the sintering of Ag particles, resulting

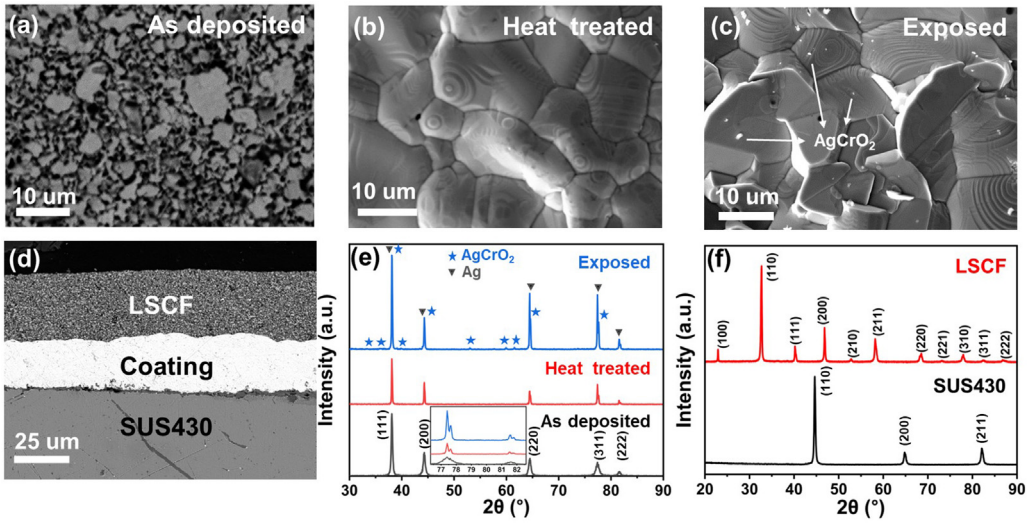

Fig. 1. (a) SEM image of the surface of the Ag coating (as deposited). (b) Surface SEM image of the Ag coating after heat treatment at 900 °C for 2 h (heat treated). (c) SEM of the Ag-coated surface after exposure to air with 3 % H_2O at 750 °C for 100 h (exposed). (d) Cross section SEM image of the exposure sample heat treated at 900 °C for 2 h in air. (e) XRD of Ag coatings as deposited; heat treated at 900 °C for 2 h; and exposed in air with 3 % H_2O at 750 °C for 100 h. (f) XRD of SUS430 base and sectional LSCF cathode material.

in a more continuous and smoother surface. The grains appear to coalesce, forming well-defined grain boundaries with a noticeable increase in grain size. This change indicates enhanced particle adhesion and reduced surface area, a critical factor for improving the coating's conductivity and stability [43]. Following 100 h of air exposure (Fig. 1c), the Ag coating further evolves. The surface remains smooth, but the coating grain boundaries become more pronounced, and there is evidence of minor grain growth. This suggests that the coating maintains its structural integrity and resists significant morphological degradation over prolonged exposure to air with 3 % H_2O. The stability of the microstructure under such conditions is crucial for the durability of the coating in practical applications [44,45].

The cross-sectional SEM image (Fig. 1d) reveals a layered structure comprising the LSCF cathode material, the Ag coating, and the SUS430 stainless steel substrate. The Ag coating layer is distinctly visible, showing uniform thickness (about 20 ± 2 μm) and good adherence to both the LSCF (about 28 ± 2 μm) and SUS430 layers (about 3 ± 2 mm). The absence of cracks or delamination at the interfaces suggests strong bonding and structural cohesion, essential for effective interconnectivity and long-term operational stability [46–48].

The XRD patterns (Fig. 1e and f) further elucidate the coatings' structural integrity and phase composition. Fig. 1e shows the XRD spectra of the Ag coatings in three states: uncalcined, calcined at 900 °C for 2 h, and after 100 h of air with 3 % H_2O exposure at 750 °C. The uncalcined coating displays characteristic peaks of metallic Ag [49,50]. After heating at 900 °C for 2 h, the peak corresponding to Ag remains, and no significant new peaks are marked, suggesting that Ag is still the dominant phase. Compared to the heat-treated sample with deposited sample, sharper peaks can be observed, which may be related to the increase in crystallinity of the Ag coating, as seen in the SEM structural changes in Fig. 1a to b. The diffraction peaks become much more intense after exposure to air containing 3 % H_2O, which might indicate an improvement in crystallinity and an increase in grain size [51]. This suggests that the sample has become more ordered and stable over time under thermal treatment [52]. 100 h of heating leads to the appearance of new phases on the surface of Ag coating, which are likely the oxides of Ag and Cr. This compound may be $AgCrO_2$, as inferred by comparing the peak values of XRD [53,54]. The Cr or Cr compounds diffused from the SUS430 substrate pass through the lattice of Ag instead of grain boundaries and react with oxygen on the surface of the coating to form the compound $AgCrO_2$, corresponding to the white bright spots present on the surface of the Ag coating in Fig. 1c. Notably, these precipitated oxides are distributed in the lattice rather than at the grain boundaries. Related literature [55,56] also indicates Cr diffuses primarily through the Ag lattice (via vacancies/interstitials) rather than along grain boundaries, as evidenced by $AgCrO_2$ formation [55] and atomic-scale diffusion mechanisms [56]. Bulk diffusion dominates over grain boundary pathways in Ag-Cr systems.

The conductivity of layered silver based oxides (such as $AgCrO_2$) is typically in the range of 10^{-2}–10^{2} S cm^{-1}, but the d^6 electrons of Co^{3+} are more likely to participate in conductivity [57]. In contrast, the d^3 electrons of Cr^{3+} may lead to lower conductivity of $AgCrO_2$, estimated to be in the range of 10^{-3}–10^{-1} S cm^{-1} (semiconductor range) [58].

Fig. 1f shows the XRD patterns of the 430 stainless steel substrate and the LSCF cathode material. The substrate shows typical peaks of ferritic stainless steel [59], while the LSCF pattern confirms the presence of the desired perovskite phase, which is crucial for its functionality as a cathode material in fuel cells [60].

In summary, the Ag coating undergoes significant microstructural refinement upon calcination, resulting in enhanced grain structure and stability. The coating maintains its integrity and crystallinity even after prolonged exposure to air with 3 % H_2O. The cross-sectional and XRD analyses corroborate these findings, highlighting the robustness and compatibility of the coating with the underlying materials.

3.2. Coating effect on oxide scale

Fig. 2(a–d) shows the cross-sectional SEM images and the corresponding EDS line scan results before and after coating the SUS430 with Ag, showing the elemental distribution along the line scan (including O, Fe, Cr, Mn and Ag). The uncoated sample, in Fig. 2(a and b), shows a uniform structure with different element distributions of Fe, Cr, and Mn, and no significant presence of O. The Ag-coated sample in Fig. 2(c and d) shows an additional Ag layer, which is visible in the SEM image and forms clear boundaries.

Fig. 2(e and f) shows that the structure of the uncoated oxide layer undergoes significant changes after being exposed at 750 °C for 100 h in the air with 3 % H_2O. The elemental distribution along the line

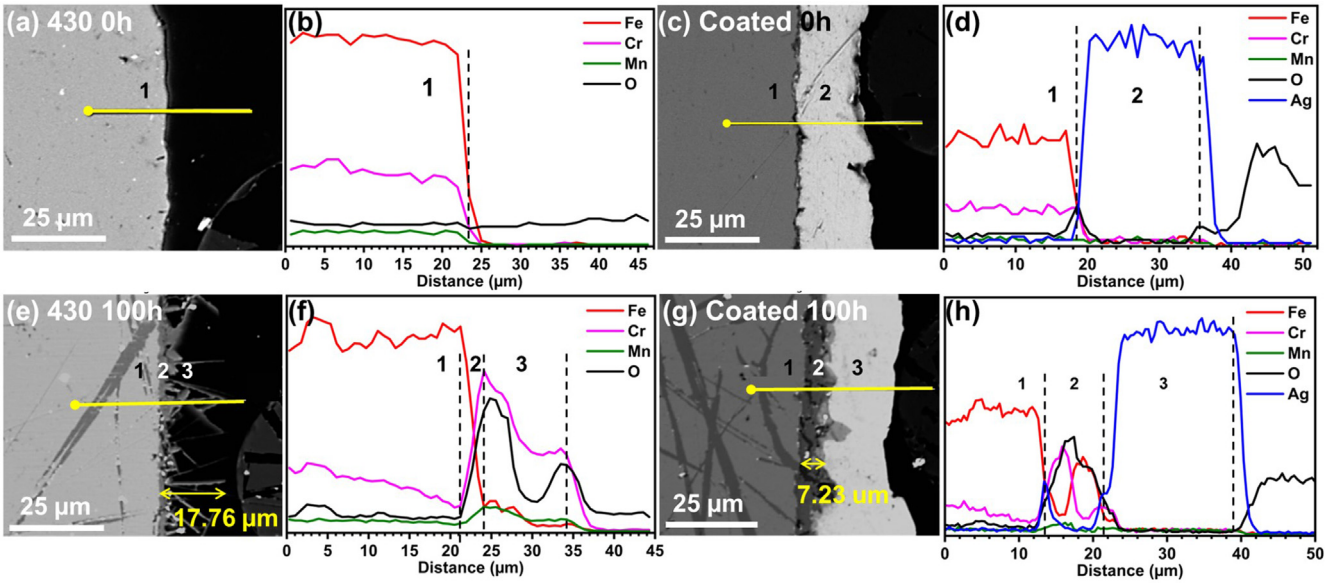

Fig. 2. SEM cross-sectional images and corresponding linescans of samples before and after exposure in air with 3 % H_2O at 750 °C for 100 h. (a) and (b) show bare SUS430 without exposure. (c) and (d) show SUS430 with a Ag coating without exposure. (e) and (f) show bare SUS430 after exposure. (g) and (h) show SUS430 with a Ag coating after exposure.

scan from the yellow dot is shown, revealing three layers: matrix, oxide, and whisker oxide growth. A whisker-like oxide layer, with the longer whisker measuring a thickness of 17.76 μm, forms on the surface, as indicated by the elevated O content observed in the line scan. The whisker-like crystals may be due to the presence of compressive stress or dislocations inside the oxide during the growth process, which promotes rapid diffusion of cations in the axial direction parallel to the surface of the oxide layer [61–63]. Based on the EDS results in Fig. 2f, the main component of the whisker-like oxide layer is Cr_2O_3. However, whisker tips may contain some $(Fe,Cr,Mn)_3O_4$ spinel phases [64] or $CrMnFeO_4$ or Cr_2MnO_4 [65]. Compared with the uncoated sample, the exposed Ag-coated sample (Fig. 2g and h) did not show the growth of whisker-like oxide scales. Instead, a structurally distinct oxide layer was present, with a thickness of 7.23 μm (yellow arrow). The oxide can be divided into two layers; from the inside to the outside there might be an oxide layer of chromia (Cr_2O_3), followed by a layer of ferrochromium spinel $(Fe, Cr)_3O_4$) [66]. In addition, the content of Ag increases at the interface between the coating and the oxide layer. This phenomenon can be attributed to the interdiffusion process between the Ag coating and steel substrate. During oxidation, Cr predominantly diffuses outward from the steel substrate to form a continuous chromia (Cr_2O_3) layer at the steel/coating interface, as evidenced by the smooth oxide/steel interface and gradual Cr depletion near this region. Concurrently, oxygen dissolved in the Ag coating reacts with the outward-diffusing chromium to form the chromia layer. Once this protective oxide layer becomes continuous, it effectively blocks the inward diffusion path, leading to the accumulation of a small amount of Ag beneath the oxide layer. The interfacial compound detected by XRD in Fig. 1e may correspond to this Ag-rich phase trapped at the interface, though its chemical state requires further verification. The Ag coating is still visible, although some diffusion may have occurred. These results indicate that the Ag coating acts as a barrier, greatly reducing the oxidation of the underlying metal during high-temperature exposure in humid environments. It helps maintain the structural integrity of SUS430 in harsh conditions.

Fig. 3 is a plot showing the thickness of oxide layers as a function of time (in hours) for different coatings on SUS430 samples exposed to high-temperature conditions. The effect of the coating on the oxidation reaction was investigated using the parabolic equation (Eq. 1) to reveal the reaction kinetics [67].

$$x = k_p t \tag{3}$$

where x is the thickness gain, k_p is the parabolic rate constant, units are expressed as $\mu m^2 s^{-1}$, t is time.

The uncoated SUS430 has a k_p value of 1.85×10^{-4} $\mu m^2 s^{-1}$, indicating a relatively high oxidation rate. Compared with other literature (3.0×10^{-4} $\mu m^2 s^{-1}$ at 800 °C [68]), the oxidation rate is higher, which may be related to the use of humid air (3 % H_2O) instead of dry air in the test [69]. Combined with the results in Fig. 2e and f, the presence

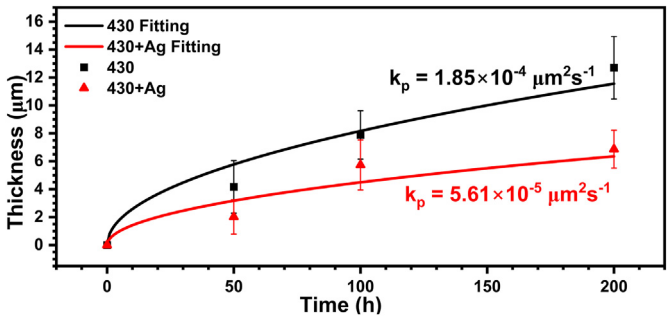

Fig. 3. The changes in oxide layer thickness and fitting curves of bare SUS430 and coated samples exposed in air with 3 % H_2O at 750 °C over 200 h. Trend lines have been added assuming parabolic kinetics.

Table 2
Comparison of electrical conductivity of different coatings from the literature.

Name	Conductivity (S cm^{-1})	Temperature (°C)	Reference
Co_3O_4	2.20	700	Brabers and Broemme [34]
Mn_3O_4	0.06	800	Logothetis and Park [35]
Mn_3O_4	0.10	800	Metselaar et al. [36]
$MnCo_2O_4$	36.00	800	Chen et al. [37]
$Mn_{1.5}Cr_{1.5}O_4$	0.07	800	Chen et al. [37]
$NiMn_2O_4$	1.40	800	Kshirsagar [38]
$NiMn_2O_4$	9.10	800	Macklen [39]
$NiFe_2O_4$	0.20	800	Lee et al. [40]
$MgMn_2O_4$	0.60	800	Keer et al. [41]
$CuMn_2O_4$	40.00	800	Kshisagar [38]
Ag	138,600.00	800	Matula [42]

of water can accelerate the diffusion of Cr and has a strong correlation with the formation of a whisker-like Cr oxide layer [70]. The Ag coating drastically reduces the oxidation rate compared to the uncoated sample. The Ag-coated SUS430 has a value of 5.61×10^{-5} $\mu m^2 s^{-1}$, which is an order of magnitude lower than the uncoated sample, indicating that the Ag coating acts as an effective barrier against oxidation, enhancing the system's high-temperature oxidation resistance. The current fitting results maintain an acceptable error margin of 0.35 %. Despite the fitting deviations, the curve clearly reveals the protective trend of the coating on the substrate. This quantitative model provides valid comparative evidence between coated and uncoated samples.

3.3. Conductivity and ASR of LSCF-based samples

The comparison in Table 2 highlights a significant aspect in this work: the use of Ag as a coating material for SOFC interconnects. The electrical conductivity of Ag at 800 °C is 4 to 5 orders of magnitude higher than that of traditional oxide coatings used in SOFC systems. The conductivity of oxide coatings typically ranges from 0.06 S cm^{-1} for Mn_3O_4 [35] to 40 S cm^{-1} for $CuMn_2O_4$ [38], whereas the conductivity of Ag reaches as high as 138,600 S cm^{-1} [42]. This stark contrast in conductivity underscores the breakthrough potential of using Ag to greatly enhance electron transport and reduce resistance in SOFC interconnects.

In order to study the adaptability of Ag coatings in cathodic environments, the conductivity and electrochemical performance of various LSCF symmetrical cell samples were investigated. The four samples presented in Fig. 4a had all undergone 100 h of operation in an oxidizing environment at 750 °C. The prolonged operation led to the formation of distinct corrosion/oxidation zones on the sample surfaces, which is the primary reason for the observed conductivity reduction. These oxidized regions exhibit low conductivity (10^{-6}–10^{-3} S cm^{-1}), consistent with literature reports on conductivity degradation caused by chromium oxide formation [71,72].

Fig. 4a presents the temperature-dependent conductivity of four different samples: uncoated SUS430, SUS430 with Ag coating, SUS430 with Ag coating and cathode material, and SUS430 with cathode material. After coating with Ag, the sample exhibited the highest conductivity across all temperatures, with a peak of 13.13 S cm^{-1} at 650 °C. The conductivity for all samples showed a decreasing trend as the temperature increased. After the addition of the cathode material LSCF, the 430 + LSCF sample was essentially identical to the uncoated SUS430, exhibiting the lowest conductivity. The 430 + Ag + LSCF sample exhibited higher conductivity than 430 and 430 + LSCF but lower than 430 + Ag, indicating that the addition of LSCF slightly reduces the beneficial effects of the Ag coating. Notably, the 430 + Ag + LSCF sample maintained moderate conductivity with minimal decline, and the contribution to the increase relative to the 430 + LSCF sample may come mainly from the Ag coating.

To assess the effect of LSCF and Ag coating on the base SUS430, the ASR was tested before exposure, as shown in Fig. 4b and c, and

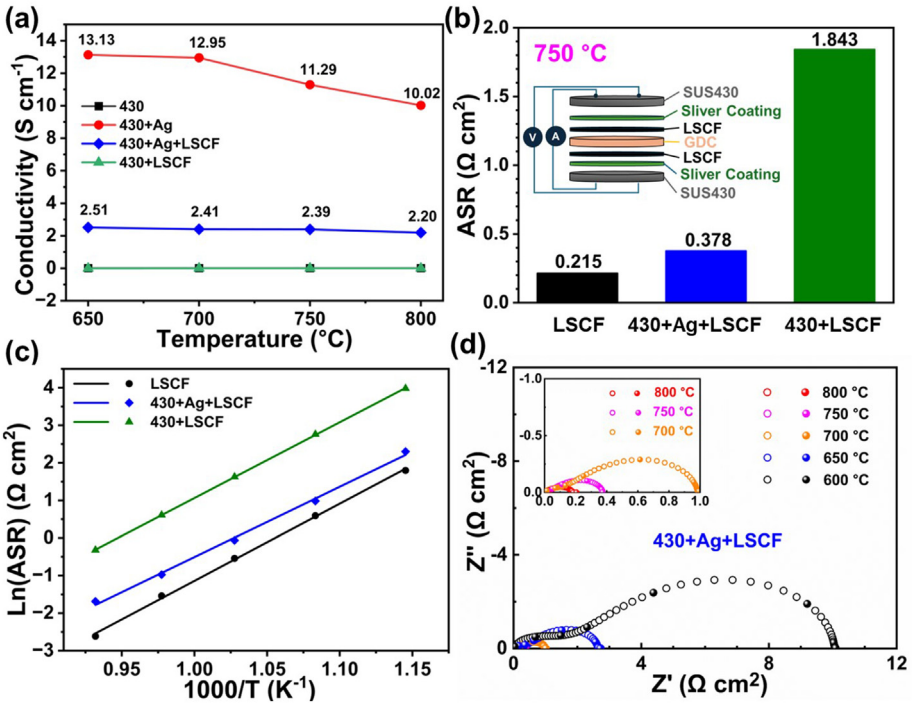

Fig. 4. (a) Conductivity curves between 650–800 °C of SUS430 (430), SUS430 with Ag coating (430 + Ag), SUS430 with Ag coating and cathode material (430 + Ag + LSCF), and SUS430 with cathode material (430 + LSCF). (b) ASR value at 750 °C and (c) Arrhenius plot of the symmetrical cell with cathode material, SUS430 with Ag coating and cathode material, SUS430 with cathode material between 600 to 800 °C. (d) Electrochemical impedance spectroscopy Nyquist plot between 600 to 800 °C for SUS430 with a Ag coating and cathode material.

the inset of Fig. 4b shows a schematic of the tested structure. The LSCF sample exhibits the lowest ASR. Samples with direct contact between cathode material and SUS430 (430 + LSCF) exhibited the highest ASR of 1.843 Ω cm^2, after coated Ag between the LSCF and SUS430 (430 + Ag + LSCF), the ASR at 0.378 Ω cm^2 decreased 79.8 % compared with 430 + LSCF. However the ASR of LSCF with GDC is only 0.215 Ω cm^2, this suggests that the increase in ASR is attributed to the interaction between the cathode material and SUS430. A similar trend is shown in the Arrhenius plots of ASR (Fig. 4c).

The Electrochemical Impedance Spectroscopy, represented by Nyquist plots (Fig. 4d), illustrates the complex impedance (Z' vs Z") for 430 bare with Ag coating and cathode material LSCF across different temperatures (600–800 °C). At higher temperatures, the impedance arcs decreased in size, indicating a lower resistance. After coating, 430 + Ag + LSCF with a smaller impedance arc than 430 + LSCF (shown in Fig. S4) suggests Ag coating positively affects interconnect electrochemical performance. Insets in these plots provide a zoomed-in view of the high-frequency region for enhanced clarity. The results demonstrate that Ag coatings significantly enhance the electrical conductivity and reduce the ASR of SUS430 stainless steel interconnects. The combination of Ag coating and LSCF (430 + Ag + LSCF) offers a balanced performance with moderate conductivity and ASR, making it a promising candidate for SOFC interconnect applications.

3.4. Coating effect on output power and stability

To further investigate the suitability and applicability of Ag as a coating for SOFC interconnects, samples consisting of LSCF single cells and interconnects were tested. The structure is schematically shown in Fig. 5c. The interconnects were mechanically fixed onto the anode-supported full cell using ceramic plates and screws. Due to the inherent brittleness of the anode substrate (diameter 2 cm), excessive pressure could not be applied during assembly to avoid fracturing the cell. This resulted in suboptimal interfacial contact between the interconnects and the cell, increasing interfacial resistance and hindering efficient charge/ion transport compared to the structure without interconnects.

Voltage and power density as a function of current density are illustrated in Fig. 5a and b for 430 + Ag + LSCF, and 430 + LSCF samples at different temperatures (700–850 °C). The performance improved with increasing temperature for all samples, with 430 + Ag + LSCF exhibiting the highest output power density and voltage across all temperatures. At 850 °C, the maximum power densities of coated sample were 0.153 W cm^{-2}, increased by 363.6 % compared with uncoated sample (0.033 W cm^{-2}).

The increase in output power may be related to two factors, which are the increase in conductivity and the decrease in ASR. The high conductivity (as shown in Fig. 4a) provided by the Ag coating accelerates the transfer of electrons from the electrode material to the interconnect and provides an effective barrier between the cathode material and the interconnect to prevent their interfacial reaction [73]. The stability of the coating is important for the SOFCs application, the resistivity results of the coated sample for 100 h of continuous testing were given in Fig. 5d. After 100 h at 750 °C, the resistivity increased from 0.124 to 0.387 Ω m, which remained relatively stable over 100 h, indicating good stability. The increase in resistivity primarily originates from the progressive thickening of the oxide layer formed at the coating–substrate interface. The oxide layer growth kinetics curve in Fig. 3 quantitatively demonstrates this correlation: During isothermal oxidation at 750 °C, the thickness increases from 3.07 μm at 50 h to 4.69 μm after 100 h. This is related to the charge carrier transport rate through the oxide layer being slower than that in both the Ag coating and Fe-Cr alloy substrate.

3.5. Coating effect on Cr diffusion to cathode

To further analyze the causes of degradation of single cell, XPS (a–c) of the surface and EDS (d–m) of the cross-section were given in Fig. 6. The XPS spectra showed Cr 2p peaks corresponding to Cr^{6+} $2p_{1/2}$, Cr^{3+} $2p_{1/2}$, Cr^{6+} $2p_{3/2}$, and Cr^{3+} $2p_{3/2}$ indicating that Cr has diffused from

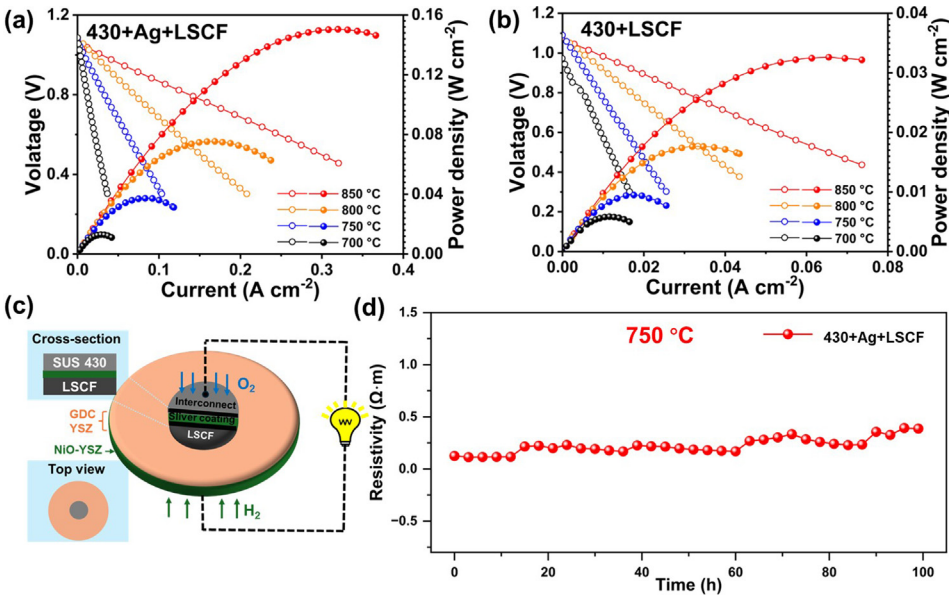

Fig. 5. I–V and I–P curve for (a) Ag coating and SUS430 (b) cell with cathode LSCF and SUS430. (c) Schematic of cell structure, coating, and interconnect during the cell test. (d) Resistivity curve of SUS430 with Ag coating and LSCF for 100 h.

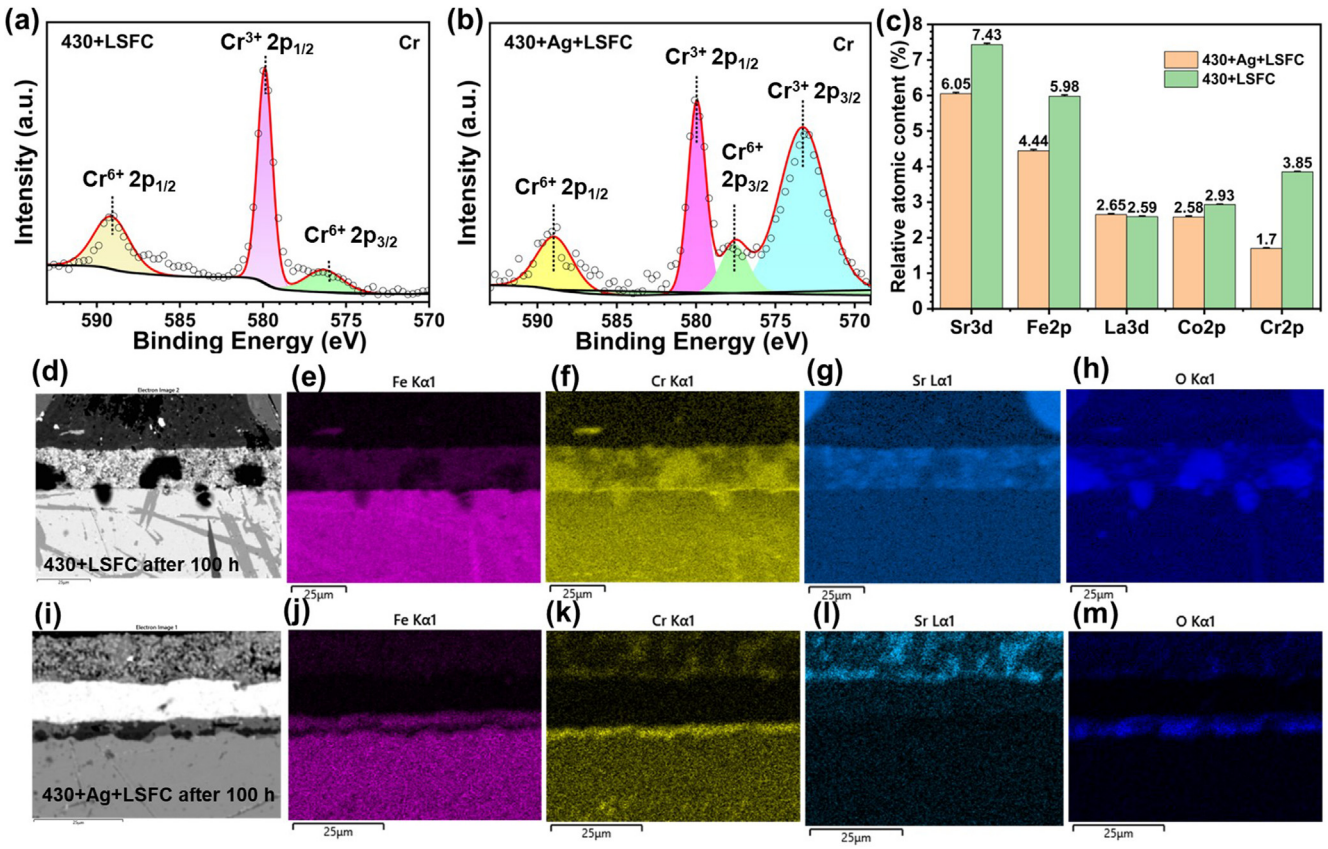

Fig. 6. XPS testing and fitting curves of (a) SUS430 with LSCF and (b) SUS430 with Ag coating and LSCF. (c) Bar chart of relative content of surface elements for SUS430 with LSCF and SUS430 with Ag coating and LSCF. EDS mapping of (d–e) SUS430 with LSCF and (i–j) SUS 430 with Ag coating and LSCF.

the interconnect to the surface of both the coated and uncoated samples. The presence of both Cr^{6+} and Cr^{3+} indicated Cr contamination on the surface. The peak at 589 eV suggests the presence of Cr in a higher oxidation state, likely Cr(VI) [74]. Combined with the EDS results, the corresponding compound consists of the elements Cr and strontium, probably strontium chromate ($SrCrO_4$) [75]. The peak value of Cr 2p matches the research of Zhang et al. [76]. Comparing Fig. 6a and b, the addition of the coating results in the appearance and enhancement of a peak at 573 eV, corresponding to Cr(III). This indicates that the presence of Ag affects the valence state of Cr, leading to a reduction from

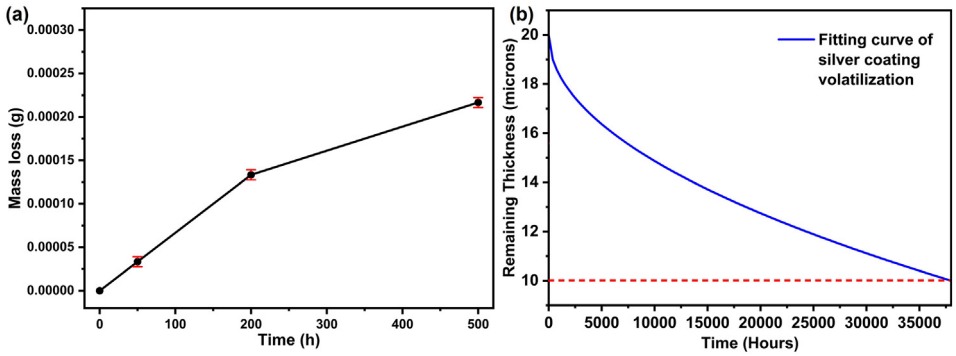

Fig. 7. (a) Mass loss curve of Ag coating at 750 °C for 50 h, 200 h and 500 h. (b) The prediction curve showing the thickness of the Ag coating decreasing from 20 μm to 10 μm at 750 °C.

higher oxidation states (Cr(VI)) to lower ones (Cr(III) or metallic Cr). The formation of new interfaces between Ag and Cr species may contribute to these shifts in binding energy and oxidation states, potentially facilitating the formation of $AgCrO_2$ [77,78].

Fig. 6c compares the relative atomic content (%) of various elements (Sr 3d, Fe 2p, La 3d, Co 2p, and Cr 2p) in 430 + Ag + LSCF and 430 + LSCF samples. The 430 + Ag + LSCF sample had higher Sr and Fe content, while the 430 + LSCF sample exhibited higher Cr content. The reduced Cr content in 430 + Ag + LSCF suggests better Cr suppression.

Cross-sectional elemental mapping after 100 h of operation (Fig. 6d–h) indicated significant Cr migration in the 430 + LSCF sample. A significant amount of oxides of Cr ($SrCrO_4$ and Cr_2O_3) was evident in the LSCF layer of the cathode material and these oxides (Cr_2O_3) were able to intrude into the interior of the interconnects at the same time, which explains the reduced conductivity of the 430 + LSCF, the elevated ASR and the reduced output power. This result was also proved by Chen et al. [79]. $SrCrO_4$ destroys the pristine morphology of the LSCF cathode. In Fig. 6d and i, the large black areas in the LSCF layer and oxide layer appear as voids. These voids are likely due to the inherent brittleness of the LSCF material and the polishing of the samples, which can cause parts of the material to fall during the grinding and sample preparation process.

The 430 + Ag + LSCF sample showed a more uniform elemental distribution with lower Cr migration in Fig. 6i–m. The Ag coating contained the Cr below the Fe oxide layer to form a stable Cr oxide layer, mitigating the mutual aggression between the cathode material LSCF and the interconnects. The reduction in ASR (Fig. 4b and c) was strongly correlated with the improved stability of the interface after coating. This detailed analysis shows that the addition of an Ag coating significantly affects the chemical state and electronic environment of Cr in the material, potentially improving its oxidation and corrosion resistance properties.

3.6. Life prediction of Ag coating

The data presented above indicate that the application of an Ag coating on SOFC interconnects can enhance electrical conductivity, reduce area-specific resistance, and improve output power, while also providing some degree of Cr diffusion prevention. However, the volatility of Ag at high temperatures is a significant issue that cannot be overlooked. To investigate the evaporation behavior of the Ag coating under high-temperature conditions, we conducted mass loss measurements of the Ag coating after exposure to 750 °C for 50, 200, and 500 h, as shown in Fig. 7a. After 500 h of exposure, the mass loss of the Ag was recorded at 0.00021 g.

Based on this data, we projected the performance of the 20-micron-thick Ag coating, prepared using the screen-printing method, under operation in 750 °C air. As shown in Fig. 7b, the model predicts that when 50 % of the coating thickness is lost (i.e., the remaining thickness is 10 μm), it would take approximately 38,000 h (around 4.3 years) of operation. This analysis suggests that despite the volatility concerns, the Ag coating could offer a reasonable operational lifespan in SOFC interconnects at elevated temperatures before significant degradation occurs.

The evaporation of Ag and its subsequent deposition on cathode and anode materials can influence the system's lifespan. Interestingly, such Ag deposition has the potential to enhance the performance of cathode materials. This view is supported by research demonstrating significant improvements in cathode performance through the incorporation of Ag nanoparticles. For instance, Zhu et al. [28] reported a Ag nanoparticle-decorated peritectic oxide electrocatalyst exhibiting ultralow area-specific resistance (0.214 Ω cm^2 at 500 °C) with exceptional stability in low-temperature solid oxide fuel cells, delivering a peak power density of 1116 mW cm^{-2} at 500 °C and maintaining 140-hour durability under 625 mA cm^{-2} operation. Additionally, Jeon et al. [80] developed an Ag/ZrO_2 nanocomposite material deposited on LSCF cathodes, with the stable electrode resistance of 0.085 Ω cm^2 after 200-hour operation at 650 °C, achieving performance levels among the highest ever recorded for nanoparticle-infiltrated LSCF cathodes. These findings indicate that Ag nanoparticles not only enhance the catalytic activity and conductivity of perovskite cathodes but also improve their adaptability to complex atmospheres. This suggests that, under controlled conditions, the evaporation of Ag could potentially be turned into an advantage for optimizing cathode performance.

Apart from the issue of Ag coating evaporation, the high cost of Ag remains a significant challenge. The trade-off between final SOFC cost and lifespan can be addressed through strategies such as optimizing coating thickness, developing composite coatings, improving coating processes, and promoting recycling and reuse. Future work should focus on minimizing Ag usage while ensuring the long-term stability and performance of interconnects, thereby achieving the optimal balance between cost and durability.

4. Conclusion

In this study, we have demonstrated the development of a novel Ag coating for SOFC interconnects, which has a dense surface and significant resistance to oxidation in humid air. The application of this coating resulted in a marked improvement in the system's conductivity, increasing by 100 fold, and a substantial reduction in the area-specific resistance from 1.843 Ω cm^2 to 0.378 Ω cm^2 at 750 °C. When applied to an SOFC single cell, the maximum power densities were enhanced from 0.033 W cm^{-2} to 0.153 W cm^{-2} at 850 °C. Additionally, the coating demonstrates certain potential in inhibiting chromium volatilization, thereby enhancing the interconnect stability. Overall, this Ag coating offers promising prospects for use in SOFC interconnects. However, the high cost of Ag remains a notable challenge. Future work should focus

on exploring strategies to reduce the cost of this coating, ensuring its economic viability for widespread application.

CRediT authorship contribution statement

Gongmei Yang: Writing – original draft, Methodology, Formal analysis. **Andrew Potter:** Writing – review & editing. **Joy Sumner:** Writing – review & editing, Supervision.

Declaration of competing interest

The authors declare that they have no known competing financial interests or personal relationships that could have appeared to influence the work reported in this paper.

Acknowledgements

This research was supported by the Centre for Energy Engineering at Cranfield University (UK). Thank you to the China Scholarship Council for their support.

Appendix A. Supplementary data

Supplementary data to this article can be found online at doi:10.1016/j.fuel.2025.136134.

Data availability statement

Data supporting this study are openly available from the following link:

https://doi.org/10.57996/cran.ceres-2730
https://dspace.lib.cranfield.ac.uk/handle/1826/23469

References

[1] Yi Y, Rao AD, Brouwer J, Samuelsen GS. Analysis and optimization of a solid oxide fuel cell and intercooled gas turbine (SOFC-ICGT) hybrid cycle. J Power Sources 2004;132:77–85.
[2] McLarty D, Brouwer J, Samuelsen S. Fuel cell–gas turbine hybrid system design part I: steady state performance. J Power Sources 2014;257:412–20.
[3] Eveloy V. Hybridization of solid oxide electrolysis-based power-to-methane with oxyfuel combustion and carbon dioxide utilization for energy storage. Renew Sustain Energy Rev 2019;108:550–71.
[4] Singh M, Zappa D, Comini E. Solid oxide fuel cell: decade of progress, future perspectives and challenges. Int J Hydrogen Energy 2021;46:27643–74.
[5] Xu Q, Guo Z, Xia L, He Q, Li Z, Bello IT, et al. A comprehensive review of solid oxide fuel cells operating on various promising alternative fuels. Energy Convers Manag 2022;253:115175.
[6] Mao J, Wang E, Wang H, Ouyang M, Chen Y, Hu H, et al. Progress in metal corrosion mechanism and protective coating technology for interconnect and metal support of solid oxide cells. Renew Sustain Energy Rev 2023;185:113597.
[7] Wu J, Liu X. Recent development of SOFC metallic interconnect. J Mater Sci Technol 2010;26:293–305.
[8] Yang Z. Recent advances in metallic interconnects for solid oxide fuel cells. Int Mater Rev 2008;53:39–54. https://doi.org/10.1179/174328007X212526.
[9] Deng J, Li Y, Tong W, Song J. Research progresses in the preparation of spinel coatings on the surface of sofc ferrite stainless steel interconnectors. In: 2021 3rd international academic exchange conference on science and technology innovation (IAECST). IEEE; 2021. p. 1113–9.
[10] Frangini S, Masci A, McPhail S, Soccio T, Zaza F. Degradation behavior of a commercial 13Cr ferritic stainless steel (SS405) exposed to an ambient air atmosphere for IT-SOFC interconnect applications. Mater Chem Phys 2014;144:491–7.
[11] Chen X, et al. Chromium deposition and poisoning of cathodes of solid oxide fuel cells–a review. Int J Hydrogen Energy 2014;39:505–31.
[12] Yang Z, Guo M, Wang N, Ma C, Wang J, Han M. A short review of cathode poisoning and corrosion in solid oxide fuel cell. Int J Hydrogen Energy 2017;42:24948–59.
[13] Zhou L, Mason JH, Li W, Liu X. Comprehensive review of chromium deposition and poisoning of solid oxide fuel cells (SOFCs) cathode materials. Renew Sustain Energy Rev 2020;134:110320.
[14] Fontana S, Amendola R, Chevalier S, Piccardo P, Caboche G, Viviani M, et al. Metallic interconnects for SOFC: characterisation of corrosion resistance and conductivity evaluation at operating temperature of differently coated alloys. J Power Sources 2007;171:652–62.
[15] Stanislowski M, Froitzheim J, Niewolak L, Quadakkers W, Hilpert K, Markus T, et al. Reduction of chromium vaporization from SOFC interconnectors by highly effective coatings. J Power Sources 2007;164:578–89.
[16] Feng Z, Zeng C. $LaCrO_3$-based coatings deposited by high-energy micro-arc alloying process on a ferritic stainless steel interconnect material. J Power Sources 2010;195:4242–6.
[17] Feng Z, Xu Y, Zeng C. Preparation and high temperature performances of$DyCrO_3$-based coatings on a ferritic stainless steel interconnect material. J Power Sources 2013;235:54–61.
[18] Goebel C, Berger R, Bernuy-Lopez C, Westlinder J, Svensson J-E, Froitzheim J. Long-term (4 year) degradation behavior of coated stainless steel 441 used for solid oxide fuel cell interconnect applications. J Power Sources 2020;449:227480.
[19] Reddy M, Chausson T, Svensson J, Froitzheim J. 11–23 % Cr steels for solid oxide fuel cell interconnect applications at 800 °C-how the coating determines oxidation kinetics. Int J Hydrogen Energy 2023;48:12893–904.
[20] Hashemi S, Dayaghi AM, Askari M, Gannon PE. Sol-gel synthesis of $Mn_{1.5}Co_{1.5}O_4$ spinel nano powders for coating applications. Mater Res Bull 2018;102:180–5.
[21] Tomas M, Asokan V, Puranen J, Svensson J-E, Froitzheim J. Efficiencies of cobalt- and copper-based coatings applied by different deposition processes for applications in intermediate-temperature solid oxide fuel cells. Int J Hydrogen Energy 2022;47:32628–40.
[22] Gannon P, Deibert M, White P, Smith R, Chen H, Priyantha W, et al. Advanced PVD protective coatings for SOFC interconnects. Int J Hydrogen Energy 2008;33:3991–4000.
[23] Omar NI, Tan KH, Taib H, Rahman HA. Electrophoretic deposited LSCF-SDCC-Ag cathode coating on ferritic stainless steel interconnect for SOFC. J Phys Ser 2017 Dec;12–3.
[24] Lowrance Y, Azmi MA, Rahman H, Zakaria H, Hassan S. A review on the solid oxide fuel cells (SOFCs) interconnect coating quality on electrophoretic deposition (EPD) processing parameters. In: AIP Conference proceedings; vol. 2339. AIP Publishing; 2021. p. 1.
[25] Brouzgou A, Demin A, Tsiakaras P. Interconnects for solid oxide fuel cells. In: Advances in medium and high temperature solid oxide fuel cell technology; 2017. p. 119–53.
[26] Majewski AJ, Dhir A. Application of silver in microtubular solid oxide fuel cells. Mater Renew Sustain Energy 2018;7:1–13.
[27] Agun L, Bakar MSA, Ahmad S, Muchtar A, Rahman HA. Influence of Ag on chemical and thermal compatibility of LSCF-SDCC for LT-SOFC. Appl Mech Mater 2015;773:445–9.
[28] Zhu Y, Zhou W, Ran R, Chen Y, Shao Z, Liu M. Promotion of oxygen reduction by exsolved silver nanoparticles on a perovskite scaffold for low-temperature solid oxide fuel cells. Nano Lett 2016;16:512–8.
[29] Kim JH, Kim JK, Seo HG, Lim D-K, Jeong SJ, Seo J, et al. Ex-solved Ag nanocatalysts on a Sr-free parent scaffold authorize a highly efficient route of oxygen reduction. Adv Funct Mater 2020;30:2001326.
[30] Sarikaya A, Petrovsky V, Dogan F. Silver composites as highly stable cathode current collectors for solid oxide fuel cells. J Mater Res 2012;27:2024–9.
[31] De Silva KCR, Kaseman BJ, Bayless DJ. Silver (Ag) as anode and cathode current collectors in high temperature planar solid oxide fuel cells. Int J Hydrogen Energy 2011;36:779–86.
[32] Pang S, Yang G, Xu J, Zhu M, Wang W, Shen X. Characterization of $SmBa_{0.5}Ca_{0.5}CoCuO_{5+\delta}$ with exsolved $CaCuO_2$-type phase as an advanced cathode material of solid oxide fuel cells. Ceram Int 2020;46:3861–5.
[33] Yang G, Xu J, Pang S, Cui M, Shen X. Tuning interfacial chemistry and electrochemical properties of solid oxide cells via cation interdiffusion. Ceram Int 2020;46:12044–9.
[34] Brabers V, Terhell J. Electrical conductivity and cation valencies in nickel manganite. Phys Status Solidi A 1982;69:325–32.
[35] Logothetis E, Park K. The electrical conductivity of Mn_3O_4. Solid State Commun 1975;16:909–12.
[36] Metselaar R, Van Tol R, Piercy P. The electrical conductivity and thermoelectric power of Mn_3O_4 at high temperatures. J Solid State Chem 1981;38:335–41.
[37] Chen X, Hou PY, Jacobson CP, Visco SJ, De Jonghe LC. Protective coating on stainless steel interconnect for SOFCs: oxidation kinetics and electrical properties. Solid State Ionics 2005;176:425–33.
[38] Kshirsagar ST. Electrical and crystallographic studies of the system $Cu_xNi_{1-x}Mn_2O_4$. J Phys Soc Jpn 1969;27:1164–70.
[39] Macklen E. Electrical conductivity and cation distribution in nickel manganite. J Phys Chem Solids 1986;47:1073–9.
[40] Lee SH, Yoon SJ, Lee GJ, Kim HS, Yo CH, Ahn K, et al. Electrical and magnetic properties of $NiCrxFe_{2-x}O_4$ spinel ($0 \le x \le 0.6$). Mater Chem Phys 1999;61:147–52.
[41] Keer H, Bodas M, Bhaduri A, Biswas A. Electrical and magnetic properties of the $MgMn_2O_4$-$MgAl_2O_4$ system. J Phys D Appl Phys 1974;7:2058.
[42] Matula RA. Electrical resistivity of copper, gold, palladium, and silver. J Phys Chem Ref Data 1979;8:1147–298.
[43] Qadir D, Sharif R, Nasir R, Awad A, Mannan HA. A review on coatings through thermal spraying. Chem Pap 2024;78:71–91.
[44] Ul-Hamid A. Microstructure, properties and applications of Zr-carbide, Zr-nitride and Zr-carbonitride coatings: a review. Mater Adv 2020;1:1012–37.
[45] Guo L, Li B, Cheng Y, Wang L. Composition optimization, high-temperature stability, and thermal cycling performance of Sc-doped $Gd_2Zr_2O_7$ thermal barrier coatings: theoretical and experimental studies. J Adv Ceram 2022;11:454–69.
[46] Liu B, An Q, Yin F, Wang S, Chen C. Interface formation and bonding mechanisms of hot-rolled stainless steel clad plate. J Mater Sci 2019;54:11357–77.
[47] Yarin AL, Lee MW, An S, Yoon SS, Yarin AL, Lee MW, et al. Failure, cracks, fracture, fatigue, delamination, adhesion, and cohesion. In: Self-healing nanotextured vascular engineering materials. Springer; 2019. p. 137–63. https://doi.org/10.1007/978-3-030-05267-6_6.
[48] Huang T, Bobyr M. A review of delamination damage of composite materials. J Compos Sci 2023;7:468.
[49] Alharthi FA, Alghamdi AA, Al-Zaqri N, Alanazi HS, Alsyahi AA, Marghany AE, et al. Facile one-pot green synthesis of Ag-ZnO nanocomposites using potato peeland their Ag concentration dependent photocatalytic properties. Sci Rep 2020;10:20229.

[50] Corsino DC, Balela MDL. Room temperature sintering of printer silver nanoparticle conductive ink. In: IOP conference series: materials science and engineering; vol. 264. IOP Publishing; 2017. p. 012020.
[51] Waseda Y, Matsubara E, Shinoda K, Waseda Y, Matsubara E, Shinoda K. Diffraction from polycrystalline samples and determination of crystal structure. In: X-ray diffraction crystallography: introduction, examples and solved problems. Springer; 2011. p. 107–67. https://doi.org/10.1007/978-3-642-16635-8_4.
[52] Zhang L, Gonçalves AA, Jaroniec M. Identification of preferentially exposed crystal facets by X-ray diffraction. RSC Adv 2020;10:5585–9.
[53] Wu Y, Chiang H, Hsiang H. $AgCrO_2$ formation mechanism during silver inner electrode and Fe-Si-Cr alloy powder co-firing in metal multilayer chip power inductors. J Mater Sci Mater Electron 2019;30:8080–8.
[54] Ouyang S, Li Z, Ouyang Z, Yu T, Ye J, Zou Z. Correlation of crystal structures, electronic structures, and photocatalytic properties in a series of Ag-based oxides: $AgAlO_2$, $AgCrO_2$, and Ag_2CrO_4. J Phys Chem C 2008;112:3134–41.
[55] Yungping HCW, Hsing-I H. $Agcro_2$ formation mechanism during silver inner electrode and Fe–Si–Cr alloy powder co-firing in metal multilayer chip power inductors. J Mater Sci Mater Electron 2019;30:8080–8.
[56] Schweizer P, Sharma A, Petho L, Huszar E, Vogl LM, Michler J, et al. Atomic scale volume and grain boundary diffusion elucidated by in situ STEM. Nat Commun 2023;14:7601.
[57] Li C, Yang B, Wei R, Hu L, Tang X, Yang J, et al. Backward diode rectifying behavior in $AgCrO_2/In_2O_3$. IEEE Electron Device Lett 2020;41:541–4.
[58] Jiu-Rong H, Xue-Fan J, Xian-Feng L. First-principles studies of helical-spin order in frustrated triangular antiferromagnet $AgCrO_2$. Acta Phys Sin 2010;59:6487–93. https://doi.org/10.7498/aps.59.6487.
[59] Yu Y, Shironita S, Souma K, Umeda M. Effect of chromium content on the corrosion resistance of ferritic stainless steels in sulfuric acid solution. Heliyon 2018;4.
[60] Grimaud A, Mauvy F, Bassat J, Fourcade S, Rocheron L, Marrony M, et al. Hydration properties and rate determining steps of the oxygen reduction reaction of perovskite-related oxides as HT-SOFC cathodes. J Electrochem Soc 2012;159:B683.
[61] Tien J, Pettit F. Mechanism of oxide adherence on Fe-25Cr-4Al (Y or Sc) alloys. Metall Trans B 1972;3:1587–99.
[62] Hindam H, Whittle D. Microstructure, adhesion and growth kinetics of protective scales on metals and alloys. Oxid Met 1982;18:245–84.
[63] Tollman RL, Gulbransen EA. Crystal morphology and mechanisms of growth of alpha-Fe_2O_3 whiskers on iron. J Electrochem Soc 1967;114:1227.
[64] Skilbred AWB, Haugsrud R. The effect of water vapour on the corrosion of Sandvik Sanergy HT under dual atmosphere conditions. Oxid Met 2013;79:639–54.
[65] Spotorno R, Paravidino D, Delsante S, Piccardo P. Volatilization of chromium from AISI 441 stainless steel: time and temperature dependence. Surf Coat Technol 2022;433:128125.
[66] Gunduz KO, Chyrkin A, Goebel C, Hansen L, Hjorth O, Svensson J-E, et al. The effect of hydrogen on the breakdown of the protective oxide scale in solid oxide fuel cell interconnects. Corros Sci 2021;179:109112.
[67] Pieraggi B. Calculations of parabolic reaction rate constants. Oxid Met 1987;27:177–85.
[68] Brylewski T, Nanko M, Maruyama T, Przybylski K. Application of Fe-16Cr ferritic alloy to interconnector for a solid oxide fuel cell. Solid State Ionics 2001;143:131–50.
[69] Chyrkin A, Huczkowski P, Shemet V, Singheiser L, Quadakkers W. Sub-scale depletion and enrichment processes during high temperature oxidation of the nickel base alloy 625 in the temperature range 900-1000 °C. Oxid Met 2011;75:143–66.
[70] Jonsson T, Pujilaksono B, Hallström S, Ågren J, Svensson J-E, Johansson L-G, et al. An ESEM in situ investigation of the influence of H_2O on iron oxidation at 500 °C. Corros Sci 2009;51:1914–24.
[71] Ishtiaq M, Ali D, Ahmad R, Muneer I, Khan TM. Tuning optical and electrical characteristics through Cu doping in spray pyrolysis fabricated Cr_2O_3 thin films. Opt Mater 2024;148:114930.
[72] Luo S, Chen B, Song M, Yi J, Yu Z, Zhang Z, et al. A novel Cr_2O_3 coated CNTs system: synthesis, microstructure regulation, and characterization. Mater Charact 2023;203:113069.
[73] Khosravi S, Abbas Q, Reichmann K. Electrochemical aspects of interconnect materials in PEMFCs. Int J Hydrogen Energy 2021;46:35420–47.
[74] Greunz T, Steinberger R, Strauß B, Stifter D. Reduction of hexavalent chromium embedded in organic insulation and corrosion inhibition layers during X-ray photoelectron spectroscopy (XPS) measurements. Corros Sci 2018;143:39–45.
[75] Zhao Y, Zhang S, Su M, Huan D, Peng R, Xia C. In-situ formed $CuFe_2O_4$ spinel coating by electroplating method for solid oxide fuel cell interconnect. Chem Eng J 2023;470:144397.
[76] Zhang Y, Xu Y, Gan L. Exsolved metallic iron nanoparticles in perovskite cathode to enhance CO_2 electrolysis. J Solid State Electrochem 2022:1–9.
[77] Lutton K, Han J, Ha HM, Sur D, Romanovskaia E, Scully JR. Passivation of Ni-Cr and Ni-Cr-Mo alloys in low and high pH sulfate solutions. J Electrochem Soc 2023;170:021507.
[78] Agrawal SG, Fimmen RL, Chin Y-P. Reduction of Cr (VI) to Cr (III) by Fe (II) in the presence of fulvic acids and in lacustrine pore water. Chem Geol 2009;262:328–35.
[79] Chen Y, Zhao Y, Zhang S, Zhang B, Su M, Wang D, et al. Supersonic spray derived Cu-Co oxide coating on SUS441 to protect the metallic interconnect and to increase stability of SOFC cathode. Int J Hydrogen Energy 2024;50:1273–81.
[80] Jeon S, Seo J, Shin JW, Lee S, Seo HG, Lee S, et al. Metal-oxide nanocomposite catalyst simultaneously boosts the oxygen reduction reactivity and chemical stability of solid oxide fuel cell cathode. Chem Eng J 2023;455:140611.

DSPACE

https://dspace.org/

Improving anti-oxidation properties of metal interconnects in solid oxide fuel cells via a dense Ag-based coating layer

Yang, Gongmei; Potter, Andrew; Sumner, Joy

2026-01-15
Elsevier
https://doi.org/10.1016/j.fuel.2025.136134
Yang G, Potter A, Sumner J. (2026) Improving anti-oxidation properties of metal interconnects in solid oxide fuel cells via a dense Ag-based coating layer. Fuel, Volume 404, Part A, January 2026, Article number 136134

Downloaded from a DSpace repository. https://dspace.org/